A FAST SIMULATION METHOD OF SILICON NANOPHOTONIC ECHELLE GRATINGS AND ITS APPLICATIONS IN THE DESIGN OF ON-CHIP SPECTROMETERS

Jun Song[*], Lin-Chun Chen, and Bo-Jun Li

Key Lab of Optoelectronics Devices and Systems of Ministry of Education/Guangdong Province, Institute of Optoelectronics, Shenzhen University, Shenzhen 518060, China

Abstract—Due to their very high integration density, echelle grating spectrometers based on silicon nanophotonic platforms have received great attention for their applications in many areas, such as optical sensors, optical communications, and optical interconnections. The design of echelle gratings requires an effective modeling and simulation technique. Though we have used a boundary integral method to accurately analyze the polarization-dependent performance of the echelle grating, it is complicated and time-consuming for the simulation due to its large size and aperiodic structure. In the present paper, we will present a faster simulation method for the grating with twice total internal reflection facets based on a modified Kirchhoff-Huygens principle with the influence of the Goos-Hänchen shift considered. On the one hand, the presented simulation results agree well with our previous results obtained by the boundary integral method when the shift can accurately be calculated using a FDTD method. On the other hand, the biggest advantage of the new method over the existing methods is that it can also provide an insightful physical explanation for many numerical results. Finally, we will effectively apply the present method to design an on-chip spectrometer with very low noise floor.

1. INTRODUCTION

Compared with other spectrum-dispersion devices, planar echelle gratings are more compact and potentially have a higher spectral finesse since they can accommodate a larger number of grating
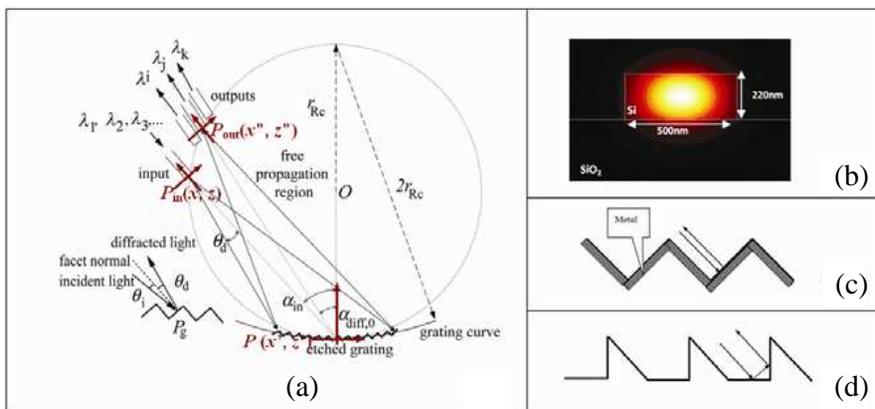
facets. Planar spectrometers based on echelle gratings have received great attention for their applications in many areas, such as optical communications [1], optical sensors [2], and optical interconnections [3].

Different technologies based on different materials have been introduced to support planar optical devices. Due to the compatibility of the fabrication technology with micro-electronics, silicon photonics has attracted a lot of interests [4–6]. Planar echelle grating spectrometers based on silicon nanophotonic platform have widely been studied in the recent years [7, 8]. However, to maintain single mode propagation along such a silicon nano-waveguide, the cross section of the waveguide needs to be very small. Then, the size of grating facets is close to the wavelength. The design of the super compact device requires an effective modeling and simulation technique.

Although progress has been made in the vectorial analysis of diffraction elements [9–13], it has been primarily limited to infinitely periodic structures. Particularly, the rigorous coupled-wave analysis (RCWA) [14] is an effective numerical method for simulating the polarization-dependent diffraction property from a planar grating. Up till now, most references to the rigorous analysis of diffraction devices have implicitly assumed infinitely periodic elements [15–18], for which the eigenfunctions are known and used in an eigenfunction expansion of the diffracted fields. However, these methods can not be applied to finite and aperiodic elements such as echelle grating spectrometers. To overcome this limitation, we recently have applied a boundary integral method (BIM) to the simulation of a diffractive element with finite size and aperiodic structure [1]. Though the BIM can be used to accurately analyze the polarization-dependent performance of the device, it is complicated and time-consuming due to its large size and aperiodic structure. Therefore, we will try to present a faster simulation method for an echelle grating spectrometer with total internal reflection facets based on the modified Kirchhoff–Huygens principle. The conventional scalar method [21] was modified by taking into account the polarization dependent Goos-Hänchen (GH) shift [19, 20] and limited groove size. The fast simulation results agreed well with our previous BIM results. Moreover, the biggest advantage of the method over the existing methods is that it can also provide an insightful physical explanation for the numerical results.

2. SIMULATION METHOD

A planar echelle grating spectrometer based on a Rowland mounting is illustrated in Figure 1(a). The field propagating from an input waveguide to the free propagation region (FPR) is diffracted by

Figure 1. (a) Schematic diagram of a planar grating spectrometers based on (b) silicon nanophotonic platform using a conventional echelle grating coated with (c) a metal at the backside and (d) a TIR grating.

each grating facet. It is then refocused onto an imaging curve and guided into the corresponding output waveguides according to the wavelengths. The grating of a planar grating spectrometer is usually coated with a metal (e.g., Au) at the backside in order to enhance the reflection efficiency (see Figure 1(c)). In order to reduce the reflection loss without the additional processing steps required for coating the backside of the grating facets with a reflecting metal, a total internal reflection (TIR) V-shaped facet was used at each grating tooth (see Figure 1(d)). Now, we will give a faster simulation method for the planar grating spectrometer with TIR facets.

For a TIR type planar spectrometer, the TIR occurs twice when the incident light impinges on an illuminated facet (see Figure 1(d)). Though intuitively no loss can be produced when a TIR occurs, our numerical calculations have shown that the loss of a TIR type spectrometer is larger than that of a metallic echelle type in many cases. Now, we will give a fast simulation method for a TIR type device based on a modified Kirchhoff-Huygens principle. The Kirchhoff-Huygens principle has been effectively used in the conventional scalar diffraction method for analyzing the crosstalk and passband performance of a planar grating device. However, the conventional scalar method cannot predict the polarization dependent loss of the device. Here we use a modified scalar method which takes into account the polarization dependent GH shift.

As shown in Figure 1(a), the output field distribution E_{image} on the surface along each output waveguide can be approximated by

Kirchhoff-Huygens' diffraction formula as,

$$E_{image}(x'', z'') = \frac{1}{2}\left(\frac{n_{eff}}{\lambda}\right)^{\frac{1}{2}} \int\limits_{grating} \frac{E_R(P)}{\sqrt{\left|\overline{PP_{out}}\right|}} (1 + \cos\theta_d) \, e^{-jk\left|\overline{PP_{out}}\right|} dl' \quad (1)$$

where $k = 2\pi n_{eff}/\lambda$ (n_{eff} is the effective refractive index of the FPR), θ_d is the diffraction angle with respect to the normal of the grating facet, $\left|\overline{PP_{out}}\right|$ the distance between a point $P(x', z')$ on the grating facet and a point $P_{out}(x'', z'')$ on the image plane, and $E_R(P)$ the reflected field distribution on any point $P(x', z')$ at the grating facets.

To obtain the image field distribution, we first derive $E_R(P)$ based on its different position on grating facets. Since the reflection occurs twice on a TIR facet, the reflected field at a point $P'(x', z')$ on one of the illuminated facets must result from another point $P(x', z')$ on the other facet of the same groove (see Figure 2). For each reflection, the reflected field can be generated by multiplying the corresponding incident field with Fresnel's reflection coefficient,

$$r_{TM}(\theta_d) = \frac{\cos\theta_d - \sqrt{(1/n_{eff})^2 - \sin^2\theta_d}}{\cos\theta_d + \sqrt{(1/n_{eff})^2 - \sin^2\theta_d}} \quad (2)$$

for a *TM* polarization, or

$$r_{TE}(\theta_d) = \frac{(1/n_{eff})^2\cos\theta_d - \sqrt{(1/n_{eff})^2 - \sin^2\theta_d}}{(1/n_{eff})^2\cos\theta_d + \sqrt{(1/n_{eff})^2 - \sin^2\theta_d}} \quad (3)$$

for a *TE* polarization. When the incident angle θ_d is less than the critical angle $\theta_c = \sin^{-1}(1/n_{eff}) \equiv \sin(n)$, the reflection coefficient r_{TM} (or r_{TE}) has a real value, which indicates that a part of the power is transmitted (or lost) whereas no phase change occurs. However, for a TIR type spectrometer based on silicon nanophotonic platform, θ_d is usually much larger than the critical angle θ_c. In this case, the reflection coefficient is a complex number. Its magnitude is always one (no transmission loss) and its phase varies depending on the polarization and the incident angle.

An important phenomenon related to the total internal reflection is the GH shift. Physically the GH shift results from the phase change of the electromagnetic field. Different incident angles and different polarizations produce different values of GH shift d (see Figure 2), which were firstly derived by Artmann with the following formulas [22],

$$d_{TE} = \frac{\lambda}{\pi}\frac{\sin\theta_d}{\sqrt{\sin^2\theta_d - n^2}} \quad (4)$$
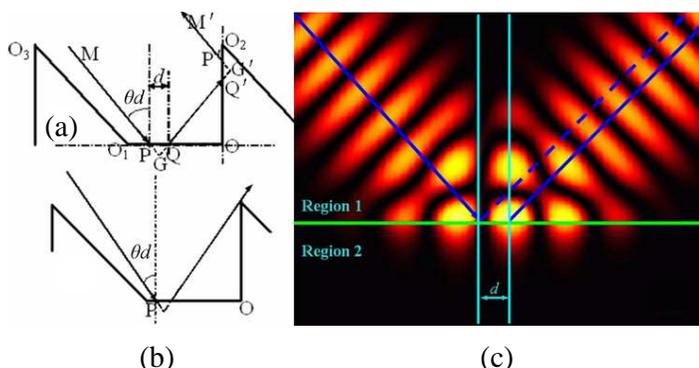
Figure 2. Main sources of the loss near a TIR facet.

$$d_{TM} = \frac{d_{TE}}{\sin^2 \theta_d \left(1 + n^2\right) - n^2} \tag{5}$$

Note that the grating period Λ also varies as the grating parameters (e.g., the diffraction order and the incident angle) change. The loss related to the GH shift depends directly on the ratio ε between the GH shift d and the grating period Λ. Apparently, when $\Lambda \gg d$, the GH shift has little effect on the loss of the spectrometer. For a straight periodic blazed grating, the grating period can be expressed as,

$$\Lambda \approx m\lambda / \left(2n_{eff} \sin \theta_d\right) \tag{6}$$

Then, the ratio ε can be approximately written as

$$\varepsilon_{TE} = \frac{2 \sin^2 \theta_d}{m\pi n \sqrt{\sin^2 \theta_d - n^2}} \tag{7}$$

for a TE polarization, or

$$\varepsilon_{TM} = \frac{2 \sin^2 \theta_d}{mn\pi \left[\sin^2 \theta_d \left(1 + n^2\right) - n^2\right] \sqrt{\sin^2 \theta_d - n^2}} \tag{8}$$

for a TM polarization. A larger ε gives a larger loss for a TIR grating spectrometer.

It should be mentioned that the theories developed in [23–25] lead to contradictory or incomplete results according to Eqs. (4) and (5). Here, we only use the Eqs. (7) and (8) as a simple model to analyze the numerical results. In the following simulations, we will give a more accurate calculation of the GH shift d_{TE} or d_{TM} by using the finite difference time domain (FDTD) method [26, 27] in terms of different incidence angles. As shown in Figure 2(c), when an incident

wavefront of the linearly polarized light makes a given angle θ_d with the surface between silicon and air, we can simulate the total reflection phenomenon by using the FDTD method. Then, we can obtain the value of the GH shift by calculating the small lateral shift d. In the following simulations, Region 1 stands for the silicon waveguide with a 3.58 index, and Region 2 stands for free space. The x-y FDTD space is 600×500 cells with a ten-cell-layer PML absorbing boundary. The cell sizes are $\Delta x = \Delta y = \lambda_0/40 = 0.038\,\mu\text{m}$. The time step is chosen as $\Delta t = 8.47 \times 10^{-17}\,\text{s}$. Note that the process does not increase extra computing amount of the simulation of the nanophotonic grating spectrometer, since the value of the GH shift at the surface of the silicon nano-waveguide is determined for a given incident angle. Therefore, we can in advance calculate the GH shift at different incident angles in terms of wavelengths and store the values as a data sheet.

Although there is no transmission loss intuitively when a TIR occurs, there are two loss sources for a TIR type spectrometer (in addition to the loss due to the light incident on a shaded facet): the effect of the GH shift, and the finite size of the facets.

As an example, we analyze potential loss sources when the incident angle α_{in} (with respect to the grating plane) equals $45°$. First, for any incident light impinging on the first facet of a TIR grating, it can not be reflected by the second facet if the distance between its incident point P and the trough point O is less than its corresponding GH shift (i.e., $|\overline{OP}| \leq d$; see Figure 2(a)). Thus, this power can not be received by the output waveguide in this situation. Secondly, when the incident angle θ_d is less than $45°$, some power illuminating on the horizontal facet can not be received by the vertical facet of the same groove due to the finite size of the vertical facet (see Figure 2(b)). Similarly, when the incident angle θ_d is larger than $45°$, some power incident on the vertical facet can not be received by the horizontal facet due to the finite size of the horizontal facet (it is re-reflected by the shaded facet and does not contribute to the desired diffraction order).

Since the vertical and horizontal facets are symmetric for a TIR facet, we only consider the incident light impinging on the horizontal facet as an example in the following analysis. When the incident light impinges at a point P on the horizontal facet, the reflected field will be produced at another point P' (whose position can be obtained using the simple ray tracing method) on the vertical facet with the same incident angle (see Figure 2(a)). When the point P' is over the top point O_2 of the vertical facet or $|\overline{OP}| \leq d$, no reflected field can be produced at point P' due to the effect of the finite size of the vertical facet (shown in Figure 2(b)) or the GH shift (shown in Figure 2(a)). Therefore, we can calculate the reflected field at point P' on the horizontal facet

using the following modified scalar formula,

$$
E_R\left(P'\right) = \begin{cases} 0; & \text{when } P_2 \text{ is over point} \\ & O_2 \text{ or } \left|\overline{OP}\right| \le d \\ r\left(\theta_d\right) r\left(90° - \theta_d\right) \exp\left(j\varphi\right) E_{in}\left(P\right); & \text{else} \end{cases} \quad (9)
$$

where $\varphi = 2\pi[n_{eff}\overline{QQ'} + 2(\overline{GQ} + \overline{G'Q'})]/\lambda$, which is used to denote the phase factor corresponding to the propagation from P to P' (see Figure 2(a)).

Since the distance $\left|\overline{PP_{in}}\right|$ between any point $P_{in}(x, z)$ on the cross-sectional line at the end of the input waveguide and any point $P(x', z')$ on the grating is much larger than the wavelength (i.e., $\left|\overline{PP_{in}}\right| \gg \lambda/n_{eff}$), the field distribution $E_{in}\left(P\right)$ at point P (see Eq. (9)) on the grating facet can be approximated by the following Rayleigh-Summerfield's diffraction formula,

$$
E_{in}\left(P\right) = \frac{1}{2}\left(\frac{n_{eff}}{\lambda}\right)^{\frac{1}{2}} \int \frac{E_{fundamental}(x, z)}{\sqrt{\left|\overline{PP_{in}}\right|}}\left(1 + \cos\theta\right)e^{-jk\left|\overline{PP_{in}}\right|}dx \quad (10)
$$

where θ is the angle between PP_{in} and the normal of the end facet of the input waveguide, and $E_{fundamental}(x, z)$ is the fundamental mode field of the input waveguide.

3. SIMULATION AND DISCUSSION

The typical structure of a silicon nanowire waveguide based on a silicon substrate is shown in Figure 1(b). The silica buffer layer should be thick enough ($\sim$5 μm) to ensure a low leaky loss. For a typical photonics application, the thickness $h = 220$ nm is fixed here, and the width $w = 500$ nm is chosen, which lies in the single mode region. The intensity profile of the propagating electric field is simulated for the channel wire waveguides (see Figure 1(b)). As an example, a planar grating spectrometer with TIR facets will be designed using the following parameters: the central wavelength is 1550 nm; the refractive indexes of silica buffer layer and α-Si : H core layer are 1.46 and 3.58, respectively; the incident angle is 45 degrees; the diffraction order is 10; channel interval is 1 nm; and the internal of output waveguides is 1 μm.

Figure 3 shows the comparison (for three different methods) of the loss of a TIR type spectrometer as a function of the diffraction order m using silicon nanophotonic platform at the central wavelength when the incident angle α_{in} is 45°. One can see that the results obtained from all three methods agree well for a larger diffraction order (e.g., $m > 11$). This is because a large diffraction order corresponds to the case of a

large facet period of the designed grating in which the scattering effect
from shaded facets and grating corners becomes insignificant on the
diffraction performance. For a lower diffraction order, the results by
using the modified scalar method with the GH shift calculated by the
FDTD are still very close to those obtained from the BIM. Therefore, as
indicated in Eq. (6), the GH shift and the finite size of the facets are two
dominating loss sources for a TIR type spectrometer. In addition, one
also sees that the GH shift calculated from Eqs. (4) and (5) is not very
accurate. However, these equations can give us an insightful physical
explanation for the numerical results. Since a larger ε gives a larger
loss for a TIR type spectrometer (see Eqs. (7) and (8)). Obviously, a
large m leads to a small ε and consequently a small loss, as shown in
Figure 3.

Figure 4 shows the loss of the grating spectrometer using the
three different methods as the incidence angle α_{in} increases when the
diffraction order is fixed as 10. The figure indicates that the analytical
Eqs. (4) and (5) induce completely contradictory results on the effect
of the incident angle, particularly for a TM polarization. However,
when we calculate the GH shift using the FDTD method, the results
obtained from the modified scalar method agree very well with those
obtained from the BIM.

(a)

(b)
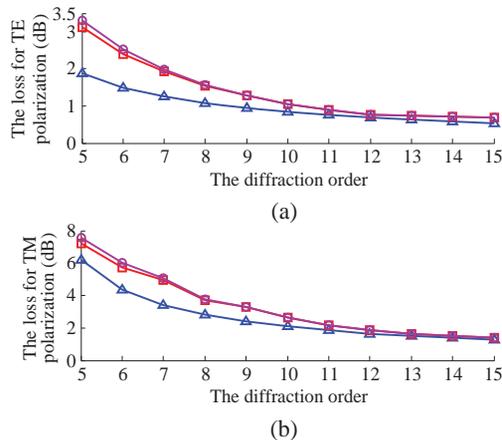
Figure 3. The loss of the TIR-grating spectrometer as a function of
the diffraction order m for (a) TE and (b) TM polarizations. Circles
are for results obtained from the boundary integral method [1]. Squares
are for results obtained from the modified scalar method with the GH
shifts calculated by the FDTD. Triangles are for results obtained from
the modified scalar method with the GH shifts calculated by Eqs. (4)
and (5).
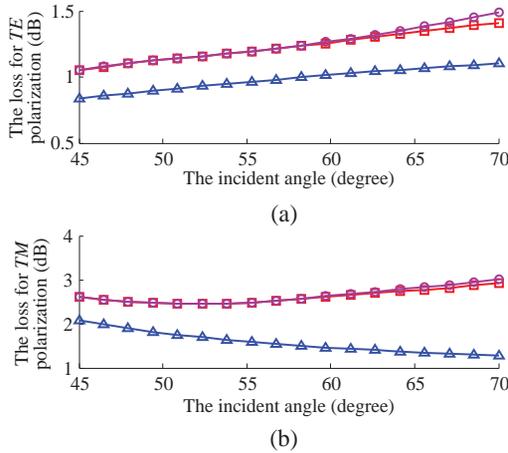
Figure 4. The loss of the TIR-grating spectrometer as the incidence angle α_{in} increases for (a) TE and (b) TM polarizations. Circles are for results obtained from the boundary integral method [1]. Squares are for results obtained from the modified scalar method with the GH shifts calculated by the FDTD. Triangles are for results obtained from the modified scalar method with the GH shifts calculated by Eqs. (4) and (5).

4. LOW NOISE SPECTROMETER DESIGN

A typical planar grating spectrometer can be considered as a linear device, whose transfer function can be expressed as [28],

$$H = \sum_{l=1}^{N} R_l b_l \exp \left[-jk \left(r_1^l + r_2^l \right) \right] \tag{11}$$

where R_l is the reflection coefficient near the lth grating facet, b_l is the ratio between the power in the lth facet and all power in the input plane, and r_1^l (or r_2^l) is the distance from the central point on the cross-sectional line at the end of the input (or output) waveguide and the central point of the lth grating facet.

As shown in Eq. (9), the GH shift and the finite size of facets are two main loss sources for a TIR-type grating spectrometer. Therefore, we can easily adjust the reflection coefficient R_l by lightly changing the size and structure of the lth grating facet. Thus, an improved transfer function for some special applications can be obtained (see Eq. (11)).

For an aberration-free imaging, the image distribution should have the same form as the fundamental mode profile of the input waveguide.

However, due to the effect of the grating diffraction, the image field distribution near each output waveguide will expend larger sidelobes into the two adjacent waveguides, which results in a large noise floor for the spectral response. Particularly, due to the small facets of gratings using silicon nanophotonic platform, it is difficult to reduce the noise floor to below 25 dB [7, 8]. However, for the application of the integrated spectrometers, it is of necessity that suppressing noise to less than 35 dB to contribute to enough measurement sensitivity [2]. From Eqs. (9) and (13), one can see that we can easily suppress the image sidelobes to less than −60 dB in theory, to give an enough space for some fabrication errors, using the present design by modulating the transfer function into an appropriate distribution.

If the number of all grating facets equals N, we will try to find the corresponding optimal reflection coefficient R_l for each facet to acquire the best performance. We consider the simulated annealing algorithm as a suitable tool for the present problem, and then define the objective function as [29],

$$f_{obj} = \frac{1}{2}\left(\frac{C}{-60\,\text{dB}}\right) + \frac{1}{2}\left(\frac{2\,\text{dB}}{L}\right) \tag{12}$$

where C is the mean noise floor of the central channel (1550 nm) and L the peak loss at the channel. For the sake of the low fabrication error, we limit the lowest reflection coefficient that each facet can attain is 5%. Thus we can search the optimal reflection coefficient of each facet in the range from 5% to 100%. We suppose that when the variety of the objective function is lower than 0.1% after ∼50 iterations, the searching process will be over.

A typical device using silicon nanowire technology has large polarization dependence which makes that a device such as a spectrometer can be only utilized for one polarization state without any compensation. In the present paper, only TE polarization considered as an example to clarify our low noise design. All parameters are the same as those in Section 3. The final reflection coefficient at different grating facets is shown in the upper-right corner in Figure 5 when the searching process is over. The final performance parameters in Eq. (12) are $C = -61.2\,\text{dB}$ and $L = 2.28\,\text{dB}$, respectively.

Figure 5 shows the spectral response at the central channel using the conventional and present design. From this figure, one can see that the mean noise floor using the design by modulating the transfer function can keep to less than −60 dB. In addition, the present design also results in an extra loss for the operational spectrum. For the central channel, the additional loss (compared with the conventional design) using the low noise floor design is about 1.92 dB, which is acceptable.
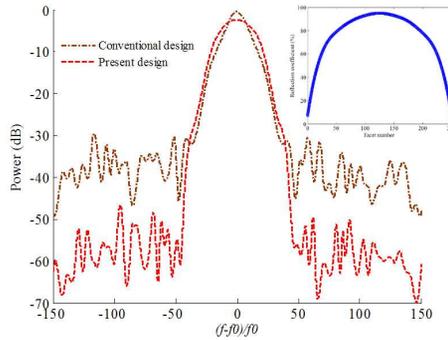
Figure 5. Spectral responses at the central channel using the conventional design (dash-dot line), and the present design (dash line).
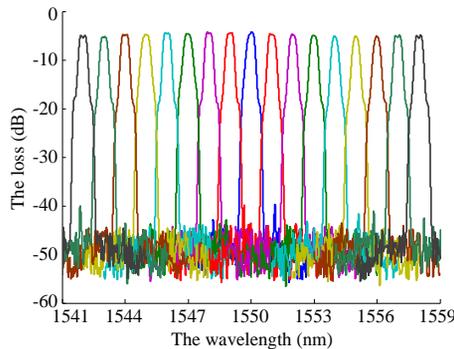
Figure 6. Measured spectral responses of a planar grating spectrometer with 17 wavelength channels.

We also fabricated and characterized the planar spectrometer using the above optimized design. Detailed design and fabrication process of the planar grating spectrometers can be found in our previous publication [1]. Figure 6 shows the spectral responses of the fabricated spectrometer for the TE polarization. The structure parameters are matched with the optimal design with low noise floor. A bit larger insertion loss compared with the numerical results (see Figure 5) is mainly due to the large scattering loss of the rough grating sidewall [1]. From the figure, one can see that the crosstalk of the fabricated device at the central wavelength is about -41.114 dB, which is also higher than that of numerical calculations (i.e., -58.92 dB) due to fabrication errors. However, the characteristic is still much better than those using conventional designs (i.e., $\sim$ -20 dB crosstalk) [1, 7, 8].

5. CONCLUSION

We have presented a fast and accurate simulation method for the planar grating spectrometer with twice total internal reflection facets based on a modified Kirchhoff-Huygens principle with the influence of the GH shift considered. When the GH shifts were calculated using the FDTD method, the proposed simulation method agreed well with the BIM. Based on the method, we can easily reshape the transfer function of the spectrometer to contribute to a low noise floor.

ACKNOWLEDGMENT

REFERENCES

1. Song, J., Y. Z. Li, X. Zhou, and X. Li, "Planar grating multiplexers using silicon nanowire technology: Numerical simulations and fabrications," *Progress In Electromagnetics Research*, Vol. 123, 509–526, 2012.

2. Song, J., Y. Z. Li, X. Zhou, and X. Li, "A highly sensitive optical sensor design by integrating a circular-hole defect with an etched diffraction grating spectrometer on an amorphous-silicon photonic chip," *IEEE Photonics Journal*, Vol. 4, 317–326, 2012.

3. Miller, D. A. B., "Device requirements for optical interconnects to silicon chips," *Proceedings of the IEEE*, Vol. 97, 1166–1185, 2009.

4. Butt, H., Q. Dai, T. D. Wilkinson, and G. A. J. Amaratunga, "Photonic crystals & metamaterial filters based on 2D arrays of silicon nanopillars," *Progress In Electromagnetics Research*, Vol. 113, 179–194, 2011.

5. Gemio, J., J. Parron, P. de Paco, J. Sacristan, and A. Baldi, "Improving silicon integrated antennas by substrate micromachining: A study of etching patterns," *Progress In Electromagnetics Research*, Vol. 117, 365–378, 2011.

6. Yao, Y. C., M. T. Tsai, P. W. Lu, C. J. Wu, and Y. J. Lee, "Effect of nanostructured architecture on the enhanced optical absorption in silicon thin-film solar cells," *Journal of Electromagnetic Waves and Applications*, Vol. 26, No. 13, 1798–1807, 2012.

7. Song, J. and J. F. Ding, "Amorphous-Si-based planar grating demultiplexers with total internal reflection grooves," *Electronics Letters*, Vol. 45, 905–906, 2009.

8. Brouckaert, J. B., W. Bogaerts, P. Dumon, D. V. Thourhout, and R. Baets, "Planar concave grating demultiplexer fabricated on a nanophotonic silicon-on-insulator platform," *IEEE Photon. Technol. Lett.*, Vol. 25, 1269–1271, 2007.

9. Sidick, E., A. Knoesen, and J. N. Mait, "Design and rigorous analysis of high-efficiency array generators," *Appl. Opt.*, Vol. 32, 2599–2605, 1993.

10. Zhang, Z. and W. Dou, "Binary diffractive small lens array for Thz imaging system," *Journal of Electromagnetic Waves and Applications*, Vol. 25, Nos. 2–3, 177–187, 2011.

11. Khaleel, S. and Ç. S. Gürel, "A new narrowband multilayer DWDM optical filter in the order of defected Fibonacci sequence," *Journal of Electromagnetic Waves and Applications*, Vol. 26, Nos. 14–15, 1930–1938, 2012.

12. Frances, J. M., C. Neipp, A. Marquez Ruiz, A. Belendez, and I. Pascual, "Analysis of reflection gratings by means of a matrix method approach," *Progress In Electromagnetics Research*, Vol. 118, 167–183, 2011.

13. Edee, M. K., I. Fenniche, G. Granet, and B. Guizal, "Modal method based on subsectional gegenbauer polynomial expansion for lamellar gratings: Weighting function, convergence and stability," *Progress In Electromagnetics Research*, Vol. 133, 17–35, 2013.

14. Wu, J. J. and B. R. Shi, "Frequency response of silicon-clad proton-exchanged channel waveguides," *Journal of Electromagnetic Waves and Applications*, Vol. 25, Nos. 5–6, 651–659, 2011.

15. Lee, D. J., S. J. Lee, W. S. Lee, and J. W. Yu, "Diffraction by dielectric-loaded multiple slits in a conducting plane: TM case," *Progress In Electromagnetics Research*, Vol. 131, 409–424, 2012.

16. Cao, T. and M. J. Cryan, "Circular dichroism in planar nonchiral metamaterial made of elliptical nanoholes array," *Journal of Electromagnetic Waves and Applications*, Vol. 26, No. 10, 1275–1282, 2012.

17. Tasinkevych, Y., "Electromagnetic scattering by periodic grating of PEC bars," *Journal of Electromagnetic Waves and Applications*, Vol. 25, Nos. 5–6, 641–650, 2011.

18. Rodríguez-Gonzalez, J. A. and F. J. Ares-Pena, "Design of planar arrays composed by an active dipole above a ground plane

with parasitic elements," *Progress In Electromagnetics Research*, Vol. 119, 265–277, 2011.

19. Baqir, M. A. and P. K. Choudhury, "On the energy flux through a uniaxial chiral metamaterial made circular waveguide under PMC boundary," *Journal of Electromagnetic Waves and Applications*, Vol. 26, No. 16, 2165–2175, 2012.

20. Dong, W., L. Gao, and C. W. Qiu, "Goos-Hänchen shift at the surface of chiral negative refractive media," *Progress In Electromagnetics Research*, Vol. 90, 255–268, 2009.

21. Hunsperger, R. G., *Integrated Optics: Theory and Technology,* 2nd Edition, 89, Springer-Verlag, 2009.

22. Artmann, K., "Berechnung der Seitenversetzung des totalreflektierten Strahles," *Annalen der Physik*, Vol. 437, 87–102, 1948.

23. Lai, H. M., F. C. Cheng, and W. K. Tang, "Goos-Hänchen effect around and off the critical angle," *J. Opt. Soc. Am. A*, Vol. 3, 550–557, 1986.

24. Lai, H. M., C. W. Kwok, Y. W. Loo, and B. Y. Xu, "Energy-flux pattern in the Goos-Hänchen effect," *Phys. Rev. E*, Vol. 62, 7330–7339, 2000.

25. Shi, J. L., C. F. Li, and Q. Wang, "Theory of the Goos-Hänchen displacement in total internal reflection," *Int. J. Mod. Phys. B*, Vol. 21, 2777–2791, 2007.

26. Kong, Y. D. and Q. X. Chu, "Reduction of numerical dispersion of the six-stages split-step unconditionally-stable FDTD method with controlling parameters," *Progress In Electromagnetics Research*, Vol. 122, 175–196, 2012.

27. Xiong, R., B. Chen, Y. F. Mao, and Q. Chen, "Thin-slot formalism for the FDTD analysis of narrow apertures having depth," *Journal of Electromagnetic Waves and Applications*, Vol. 26, Nos. 14–15, 1857–1863, 2012.

28. Shi, Z., J. J. He, and S. He, "An analytic method for designing passband flattened DWDM demultiplexers using spatial phase modulation," *Journal of Lightwave Technology*, Vol. 21, 2314–2321, 2003.

29. Mantawy, A. H., Y. L. Abdel-Magid, and S. Z. Selim, "A simulated annealing algorithm for unit commitment," *IEEE Transactions on Power Systems*, Vol. 13, 197–204, 1998.